CFD ANALYSIS OF A THERMAL MIXING IN A SUBCOOLED WATER POOL UNDER A HIGH STEAM MASS FLUX

Hyung Seok Kang and Chul Hwa Song
Korea Atomic Energy Research Institute, Korea

Abstract

A CFD (Computational Fluid Dynamics) benchmark calculation for a steam blowdown test was performed for 30 seconds to develop the methodology for a numerical analysis of the thermal mixing between steam and subcooled water and to apply it to APR1400 (Advanced Power Reactor 1400MWe). In the CFD analysis, the steam condensation phenomenon by a direct contact was simulated by the so-called condensation region model. Thermal mixing phenomenon in the subcooled water tank was treated as an incompressible flow, a free surface flow between the air and the water, a turbulent flow, and a buoyancy flow. The comparison of the CFD results with the test data showed a good agreement as a whole, but a small local temperature difference was found at some locations. The commercial CFD code of CFX4.4 together with the condensation region model can simulate the thermal mixing behavior reasonably well when a sufficient number of mesh distributions and a proper numerical method are adopted.

Introduction

The experimental and CFD research for an unstable steam condensation in a DCC (Direct Contact Condensation) which may be developed in the IRWST (In-containment Refueling Water Storage Tank) of APR1400 were performed [1-6]. An unstable steam condensation may damage into the IRWST wall [7-9]. The reason of unstable steam condensation may be the fluctuation of the interface between the steam and the condensed water when the temperature of an entrained water flowing into the steam was increased [4,8]. Therefore, the prediction of the entrained water temperature and thermal mixing pattern is important. The thermal mixing experimental program was performed to understand and to generate data for the thermal mixing phenomena induced by a steam ejection into the subcooled water in the APR1400 IRWST to prevent an unstable steam condensation being developed due to the locally increased water temperature [1-3].

In the CFD analysis, the numerical methodology which can predict the local and global thermal mixing in the tank was developed based on a comparison of the CFD results with test data. The present commercial CFD codes do not have the model of the DCC [10], and the development of a numerical model for the DCC has been restricted to an ideal flow [11]. Thus, a steam condensation region model was developed based on the water temperature data around a steam jet to simulate the DCC [4-6,12]. The calculated temperature and velocity of the condensed water and the entrained water from the condensation region model were used as the boundary conditions for a thermal mixing CFD analysis [4-6].

The comparison of the CFD results with the test data of a transient discharge of the high steam mass flux showed a good agreement as a whole, but some small temperature differences between the CFD results and the test data were shown at some locations of the upper region beside the sparger in the tank [4,6]. These differences may have arisen from an insufficient mesh distribution generated in the grid model to resolve the flow field of the jet flow at the analogous and an elevation above the sparger discharge head or an improper selection of the numerical model. The unique difference between the CFD results and the test data was the increased time of the stagnant water temperature at the high upper region [4,6]. Therefore, we investigated the effect of the grid and the numerical model sensitivity in the CFD calculations.

Thermal Mixing Test [2,3]

The thermal mixing test was performed by changing the steam mass flux and the tank water temperature (Table 1) according to the quasi steady and transient states. In this study, only a transient state test was considered.

The thermal mixing experimental facility was modified from the B&C Loop which consists of a pressurizer, a steam discharge line, a subcooled water tank, a steam sparger, and a steam generator (Fig. 1). The pressurizer supplied high pressure saturated steam at 150 bar into the subcooled water tank through the steam discharge line and the sparger. The subcooled water tank simulated the IRWST of the APR1400 and a small modified prototypic steam sparger was installed. The sparger at the discharge hole side, 64 at 1 cm in diameter (4 rows, 16 holes/row), were made of a 6 inch schedule 40S pipe and the diameter of the pipe just above the discharge holes was reduced to 2 inch. The bottom hole of a 2.5 cm diameter and the vent area of the LRR (Load Reduction Ring) were blocked in the test. These changes were intended to provide the steam flux for a long time in the test. The vertical distance between the bottom of the tank and the bottom of the sparger was set to be 0.9 m. The diameter of the tank was 3 m and it had a height of 4 m. The measurement locations of the temperature and the pressure along the steam line were shown in Fig. 1.

Eight thermocouples to measure the temperature of the steam and the entrained water flowing into the steam were installed in the tank, and two measurement rigs of 27 thermocouples were installed to obtain the thermal mixing pattern. The second rig was installed to observe the extent of the thermal mixing along the circumferential direction in the tank. The locations of the temperature measurements in the tank were shown in Fig. 2. The uncertainties of each measurement are shown in Table 2, and the overall uncertainty of the test was 13.1% [13].

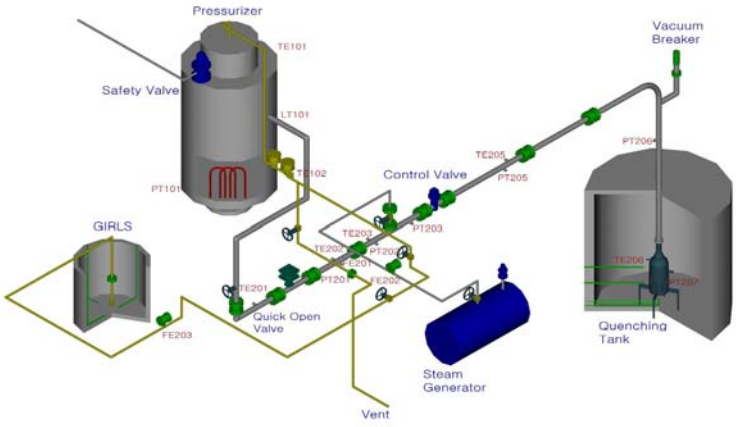

Fig. 1 Schematic Diagram of the Experimental Facility

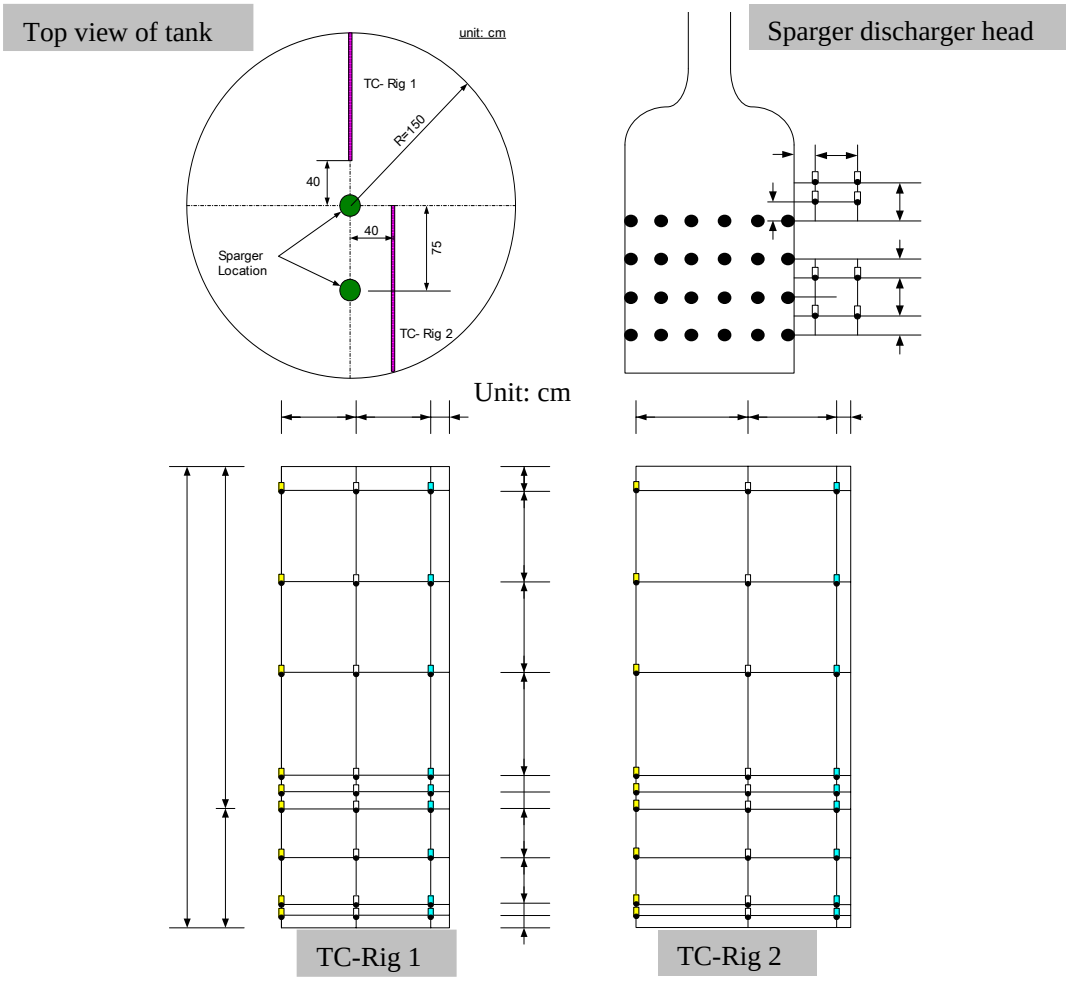

Fig. 2 Temperature Measurement Locations

Table 1 Thermal Mixing Test Conditions [2,3,13]

PZR Pressure	Steam Mass Flux	Water Temp. in Tank
150 bar	250~1600 kg/m^{2}sec	20~90 ^{o}C

Table 2 Information on the Measurement Devices [2,3,13]

Measurement Variable	Number	Uncertainty
Temperature	67	±0.7%
Static Pressure	7	±1.6%
Differential Pressure (Flowmeter)	1	±2.6%

The selected test result for the CFD benchmark calculation was a transient case for 60 seconds with the initial pressurizer pressure of 150 bar and the initial tank water temperature of about 26 ^{o}C [2,3,13]. The pressure and the temperature variation from the pressurizer to the sparger are shown in Fig. 3. The steam pressure (PT205) at the back side of the control valve was abruptly decreased because the flow path in the control valve was narrow and complicated. The steam mass flux was also shown in Fig. 3. The discharged steam may condense at about 5~8cm in the radial direction [14,15]. The temperature of the condensed water could be deduced from the temperature of TC712 and TC718 even though the steam jet, based on the boundary layer theory, did not directly flow into the those locations [16]. The temperature around the sparger (TC713, TC716) started to increase at about 17 seconds because the condensed water returns to the sparger discharge holes after a collision with the tank wall as time passed. These temperature distributions could give useful information of the entrained water which could directly affect the steam condensation [7-9]. From the temperature variation of TC646 and TC727 which represented one of the comparison results for the TC-Rig 1 with TC-Rig 2, we founded that the thermal mixing in the tank showed an almost axisymmetric pattern.

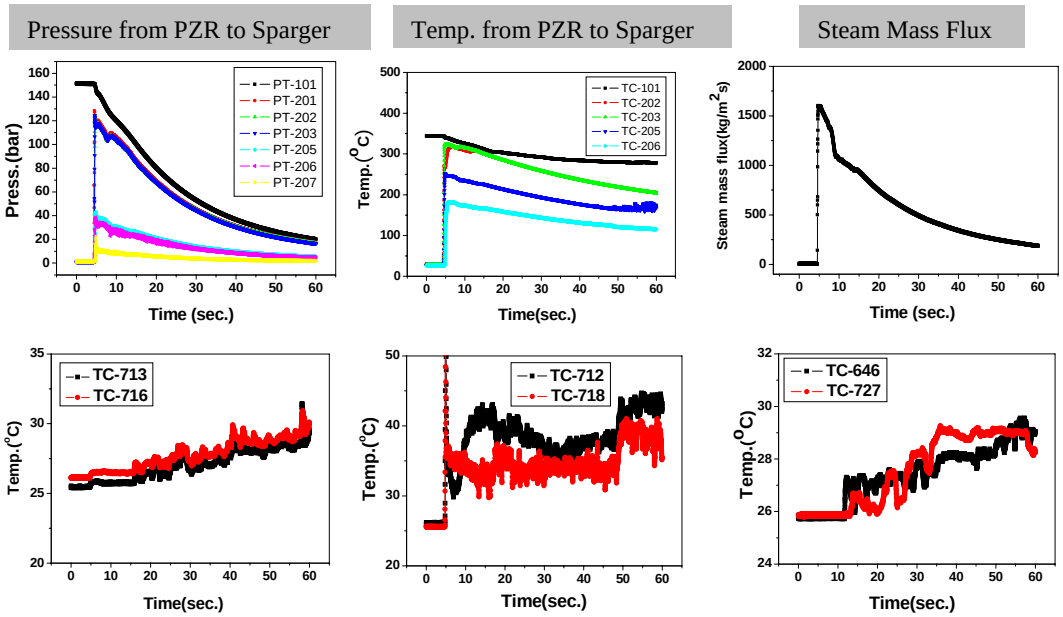

Fig. 3 Experimental Results

CFD Analysis

Critical Flow and Condensation Region Model

In the thermal mixing test, the saturated steam at about 10 bar inside the sparger was initially discharged into the water at 26 ^{o}C at 1 bar in the tank. A choking was likely to happen at the location of the sparger holes during this situation. The discharged steam flowed into the water in the tank as a jet flow, and then it was quickly condensed to water in a short time and length by a direct contact condensation [14,15]. The numerical modeling for this condensation process was so difficult that we used the steam condensation region model in which the steam was perfectly condensed to water within the steam penetration length [4-6,12]. The penetration length, Eq. (1), was defined as a function of the steam mass flow, a discharge hole diameter, and the temperature and pressure of the subcooled water [14,15]. The calculated penetration length of the steam discharged from the surface holes of 1 cm in

diameter was about 5.3 cm. The width of the jet at the end of the penetration length can be calculated as 1.2cm by use of Eq. (2), but this was only an approximated value based on the boundary layer theory, especially for the region far from the source of the jet [16]. For the entry region of the steam jet, the width in Eq. (2) was defined as the location of a half of the magnitude velocity at the center line in the jet flow. Based on the above correlations and assumptions, the condensation region model without considering the various velocity profiles was established as in Fig. 4. It was assumed that the entrained water located at above and below the condensation region model must flow into the condensation region along the normal direction, and only the condensed water leaved the outlet of the condensation region uniformly with the same velocity and temperature even though the estimated velocity profile showed a variation along the sparger discharge holes. According to the CFD calculation by considering the various velocity profiles, there is no big difference in the CFD results [4,6].

The mass flow rate of the condensed water, m_{cond}, and the entrained water, $m_{entrain}$, at the outlet of the condensation region (Fig. 4) was calculated from the mass, momentum, and energy conservation law, Eqs. (3), (4), and (5), over the condensation region [4,5,6]. The measured mass flow rate of the steam in the test facility was used as the steam velocity through the discharge holes with an assumption of a steam quality of one for solving the equations. And also, to solve Eq. (4), we must know the temperature (T_e) and pressure (P_e) of the steam at the locations of the holes. To get them, the pressure, density, and enthalpy of the steam at the surface of the holes were calculated by the isentropic relation of an ideal gas [17,18] by assuming that the choking phenomenon was developed. In these relations, the static pressure and the static temperature used the test data of PT207 and the saturated temperature at the pressure of PT207. The velocity and the enthalpy of the condensed water were obtained by using an assumed density value at 1.22 bar (P_∞), the hydraulic pressure at the length of the submergence in the tank. And also, the vertical momentum flow of the entrained water was cancelled out because we assumed that only the entrained water flows in the normal direction at the upper and lower boundaries. The pressure on the surface between the holes was also assumed to be 1.22 bar. The calculated values of the velocity and temperature of the condensed water were within 5% for the iteration errors in the energy equation as shown Fig. 5. With these values, CFX4.4 calculated the thermal mixing between the condensed water and the subcooled water in the tank by using a turbulent model and some other models.

$$\frac{x_c}{r_o} = \frac{\left[20.57\left(\frac{G_o}{G_s}\right)^{0.713}\right]}{\left[\left(\frac{\rho_\infty}{\rho_s}\right)^{0.384} B^{0.801}\right]} \qquad B = \frac{\left(h_f - h_\infty\right)}{\left(h_s - h_f\right)} \tag{1}$$

$$\frac{width}{x} = \tan 13^o \tag{2}$$

$$\dot{m}_e + \dot{m}_{entrain} = \dot{m}_{cond} \tag{3}$$

$$P_e A_e + P_\infty(\pi DH - A_e) + \rho_e V_e^2 A_e = P_{cond} A_{cond} + \rho_{cond} V_{cond}^2 A_{cond} \tag{4}$$

$$\dot{m}_e h_e + \dot{m}_{entrain} h_{entrain} = \dot{m}_{cond} h_{cond} \tag{5}$$

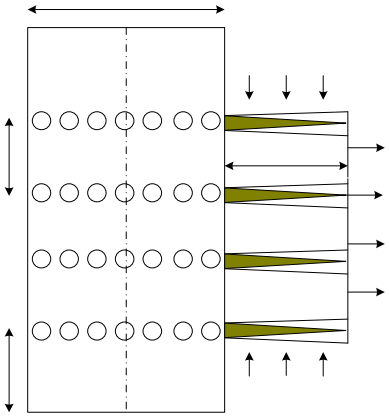

Fig. 4 Steam Condensation Region Model

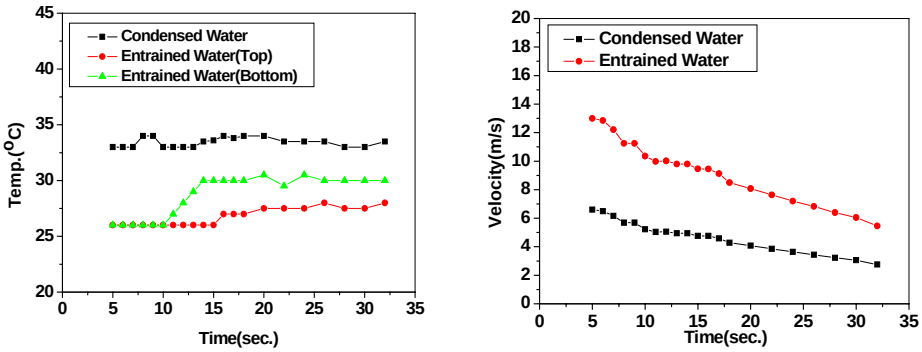

Fig. 5 Boundary Conditions for CFD Calculation

Grid Models and Boundary Conditions

A multi-grid with an axis symmetric condition for simulating the sparger and the subcooled water tank for the CFD calculation was generated (Fig. 6). The axis symmetric model was introduced because the flow pattern in the tank was estimated to vary a little in the circumferential direction (Fig. 3) and it could reduce the computational time. The grid model was generated by considering 27 thermocouple locations to read the calculation results easily. The meshes were more densely distributed around the condensation region and the initial air/water interface region than the other regions to accommodate the high velocity and temperature gradients. The air outlet region of the tank was extended in an the upward of 0.5m to move the fully developed condition imposed by applying the pressure outlet condition into the downstream of the flow field. The sensitivity calculations of the mesh distribution and the numerical method were performed (Table 3). Three cases used only the different mesh distributions in the grid model by using the same upwind 1st method [10,19] for a convection term discretization. In case 1, a total of 9,588 cells were generated, and the first grid from the right wall was located at the position of 100~300 of y+. In the second case for the sensitivity study, the mesh distribution was rearranged based on the comparison results between the CFD data of case 1 and the test data. A total of 23,835 cells and 12~50 of y+ were generated to predict the temperature close to the test data even though the computation time took longer than that of case 1. Especially, more meshes were distributed at around the jet flow and a region near to the wall. Case 3 grid model

had 31,020 cells and 12~50 of y+. The meshes of case 3 were more densely located at the transition region in the upper region of the tank than those of case 2. In case 4, the same mesh distribution of case 1 was used whereas the numerical model of the convection term discretization was changed to the quick scheme. In Table 3, the total cell number did not agreed with the value of the horizontal time vertical cells because the meshes inside of the sparger were not generated.

Table 3 Grid & Numerical Model Senetivity Calculation

	Cell No.	Horizontal×Vertical	Convection Term Discretization
Case 1	9,588	63×160	Upwind 1st
Case 2	23,835	63×160	Upwind 1st
Case 3	31,020	63×160	Upwind 1st
Case 4	9,588	63×160	Quick

The inlet boundary condition, the Dirichlet condition [10], was set at the end of the steam condensation region with a time dependent velocity and temperature as shown in Fig. 5. The values of the turbulent properties at the inlet were set as a high intensity [10] because the eddy motions were actively generated when the steam passed through the discharge holes. The pressure outlet boundary conditions, the Neumann condition [10], were set for the tanks upper region, which only allows for the outflow of air. The outlet regions for the entrained water were applied to the upper and lower region of the steam condensation regions by a negative value of the velocity with the inlet condition in the CFX4.4. The symmetry condition is applied to the center of the sparger pipe line.

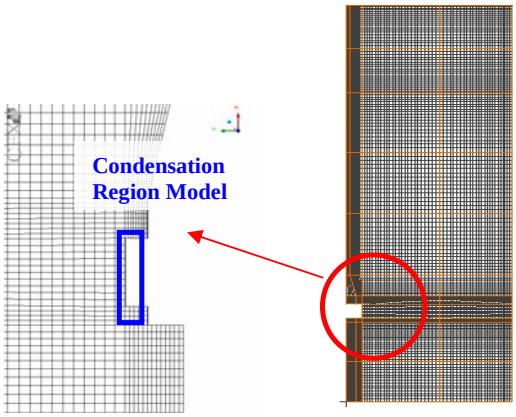

Fig. 6 Grid Model for CFD Calculation

Flow Field Models and Governing Equations [10]

Thermal mixing phenomenon in the subcooled water tank was treated as an incompressible flow, a free surface flow of air between the water, a turbulent flow, and a buoyancy flow. Therefore, the governing equations used in this study were the Navier-Stokes and energy equations with a homogenous multi-fluid model. The turbulent flow was modeled by a standard k-ε turbulent model, and the buoyancy was modeled by the Boussinesq approximation. In the homogenous model, the inter-phase mass and heat transfer were neglected. Each transport quantity in the governing equations except for the volume fraction was summed over all the phases to give a single transport quantity. The

surface sharpening algorithm was also used to treat the numerical diffusion at the interface region effectively. The finite difference scheme for each transport equation was a hybrid method except for the pressure and the volume fraction equation. The central and the upwind difference scheme were used for the pressure and the volume fraction equations, respectively. As a calculation method, 60~100 iterations were performed with the time step of 0.001~0.05 seconds until the mass, enthalpy, and velocity residual for the water reached the value of 1.0E-03 [4,5.6.12].

$$\frac{\partial}{\partial t}(r_\alpha \rho_\partial) + \nabla \bullet (r_\alpha \rho_\partial V_\alpha) = 0 \tag{6}$$

$$\frac{\partial}{\partial t}(r_\alpha \rho_\partial V) + \nabla \bullet \left(r_\alpha \left(\rho_\partial V_\alpha \otimes V_\alpha - \mu_\alpha \left(\nabla V_\alpha + (\nabla V_\alpha)^T \right) \right) \right) = r_\alpha (\mathrm{B} - \nabla P_\alpha) \tag{7}$$

$$\frac{\partial}{\partial t}(r_\alpha \rho_\partial H_\alpha) + \nabla \bullet (r_\alpha (\rho_\partial V_\alpha H_\alpha - \lambda_\alpha \nabla T_\alpha)) = 0 \tag{8}$$

$$\frac{\partial}{\partial t}(\rho k) + \nabla \bullet (\rho V k) - \nabla \bullet \left[\left(\mu + \frac{\mu_T}{\sigma_k} \right) \nabla k \right] = P + G_{buoy} - \rho \varepsilon \tag{9}$$

$$\frac{\partial}{\partial t}(\rho \varepsilon) + \nabla \bullet (\rho V \varepsilon) - \nabla \bullet \left[\left(\mu + \frac{\mu_T}{\sigma_\varepsilon} \right) \nabla \varepsilon \right] = C_1 \frac{\varepsilon}{k} P - C_2 \rho \frac{\varepsilon}{k} \tag{10}$$

$$\rho = \sum_{\alpha=1}^{N_p} r_\alpha \rho_\alpha \,,\; V = \frac{1}{\rho} \sum_{\alpha=1}^{N_p} r_\alpha \rho_\alpha V_\alpha \tag{11}$$

$$\mu_T = \sum_{\alpha=1}^{N_p} r_\alpha \mu_{T\alpha} \,,\; \mu_{\alpha,eff} = \mu_\alpha + \mu_{T\alpha} \tag{12}$$

$$G_{buoy} = -\frac{\mu_T}{\sigma_T} \beta g \bullet \nabla T \tag{13}$$

$$\rho = \rho_o [1 - \beta (T - T_o)] \tag{14}$$

Discussion on the CFX Results

The velocity vector, temperature distribution, and the comparison of the test data with the CFX results at some locations of the temperature measurement according to the cases in the tank were shown in Figs. 7~ 10. In the sensitivity calculation, all the velocity profile and thermal mixing patterns were similar to each other regardless of the cases.

Fig. 7, (a) showed the total velocity profile in the tank at 6 seconds and Fig.7, (b) showed the velocity profile, especially the circulation developed above and below the condensed water jet, at 35 seconds. It was shown that the condensed water discharged from the condensation region model easily collided with the tank wall in a very short time because the velocity of the condensed water was about 6 m/s and the distance between the sparger and the tank side wall was 1.5 m. After the collision, some of the condensed water moved upward to the interface of the air and water along the wall, and then changed its direction due to a gravity force. The rest of the downward flowing water also moved along the wall and collided once again with the bottom wall, and then it turned to the sparger. The secondary flow around the condensation region was developed because of the strong momentum of the condensed water and the entrained water.

Fig. 8 showed that the temperature distribution depending on the cases was varied according to the flow pattern as time passed. The temperature around the main flow path of the condensed water increased by 2~3 ^{o}C from the initial water temperature because of a thermal mixing between the condensed water and the tank water which happened during the stream of the condensed water. From

the figures, we can see that the temperature around the sparger increased gradually and it may have an adverse effect on a stable steam condensation. Especially, the temperature in the lower region, below the sparger discharge head, increased quicker than that of the upper region. The temperature distribution from 6.0 to 15.0 seconds showed a typical circulation in the tank. It was because the condensed water discharged from the sparger flowed upward and downward, and then it turned towards the side region and then changed its direction into the sparger. As time passed, Fig. 8 showed that one of the flows in the upper region moved upward again with a 45^{o} angle and reached the top of the tank. In fact, this upward flow was only a virtual display in the CFD results, and that region was actually an air location area in the tank. This confused display arose from a characteristic of the VOF method where all the governing equations except for each phase of the volume fraction were solved by using the average value of both phases.

The comparison results of cases 1~2 for the temperature contours showed that the thermal mixing process of case 1 was developed faster than that of case 2, and there were some different temperature distributions around the jet flow at 6 seconds. The comparison results of cases 2~3 almost showed the same results for the whole temperature distribution, but locally they showed a very small temperature profile difference. This phenomenon of a different temperature distribution depending on the number of mesh cells was due to use of the Upwind 1^{st} scheme for the convection term. If the cell is not aligned to the flow field when using the upwind scheme, the results of the flow field are dependent on the mesh distribution [19]. Therefore, a grid sensitivity calculation should be performed when solving an impinging jet with an upwind scheme. Case 4 used the same grid model but changed the Upwind 1^{st} scheme to a QUICK scheme [10,19]. The results of case 4 showed a different thermal mixing pattern, especially for the temperature distribution at 6 and 8 seconds. These temperature results were regarded as unreasonable because the accuracy of the quick scheme may be deteriorated for a complicated flow field [19].

A comparison of the temperature test data with the CFX results for 30 seconds at 6 thermocouple locations was shown in Fig. 9. These locations were expected to represent the characteristic thermal mixing pattern in the tank. It was shown that the trend of the temperature variation of the test and the CFD results were very similar as a whole, and the CFD results were higher than those of the test by 1~3 ^{o}C. It can be explained by the fact that the condensation region model in the CFD analysis used the concept of an area average, but the thermocouple measured the local phenomena.

The temperature distribution at the front of the jet flow (TC705), only in the upper region of the jet flow (TC706), the upper and lower region near the right wall (TC737, TC733), and the high upper region of the middle part (TC728, TC729) were shown as a function of the time (Fig. 9). The temperature comparison between the CFD results and the test data at TC705 showed that the temperature variation trend of the four cases were almost the same, and all the CFD results were higher than those of the test data by 2~3 ^{o}C. In the comparison results at TC706, the CFD results of the four cases predicted the test data well, but the results of case 3 were closer to the test data than those of the other cases. In case 3, the peak value at about 5 seconds and the trend of the temperature increase were very similar to the test data. In the comparison results at TC737, for all the cases CFD results also predicted the temperature trend of the test data well, but the CFD results overestimated the peak value at about 6 seconds and it could not simulate the temperature fluctuation phenomena. This may be a numerical diffusion or because we used the axis symmetric condition so that the temperature of the condensed water in the circumferential direction was constant. Therefore, the CFD results could not simulate the complicated local thermal mixing inside the upward flow along the right wall. However, for all the cases the CFD results at TC733 predicted the test data including the peak value well. From these results, we can see that the temperature distribution at the upper region may have three local dimensional effects. The comparison results at TC728 and TC729 showed that the starting time of the temperature increase in the CFD results was faster than those of the test data. This means

that the condensed water in the CFD analysis arrives at this region quicker than that of the test. And also, it depends on the numerical method of the convection term discretization. The results of case 4 by using the QUICK scheme were closer to the test data.

However, for all the cases the CFD results had a tendency of an over prediction when compared to the test data. This may be because CFX4.4 used the Reynolds Analogy concept [17,20], however this analogy may fail for an impinging jet flow with a large pressure drop [20].

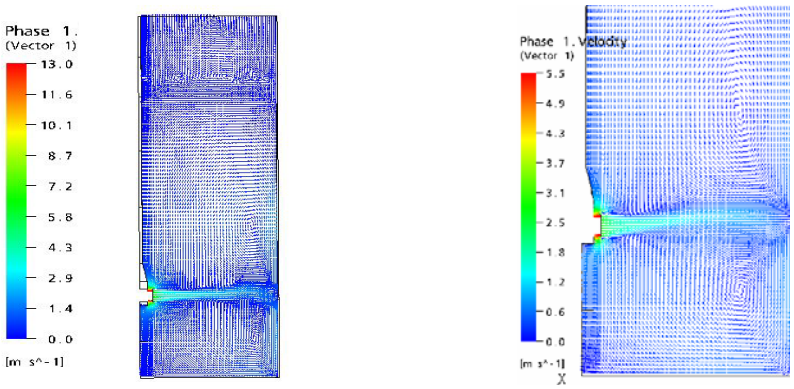

(a) 6 sec. (b) 35 sec.

(Experiment starts at 5 sec.)

Fig. 7 Velocity Profiles of the CFD Results (Case 1)

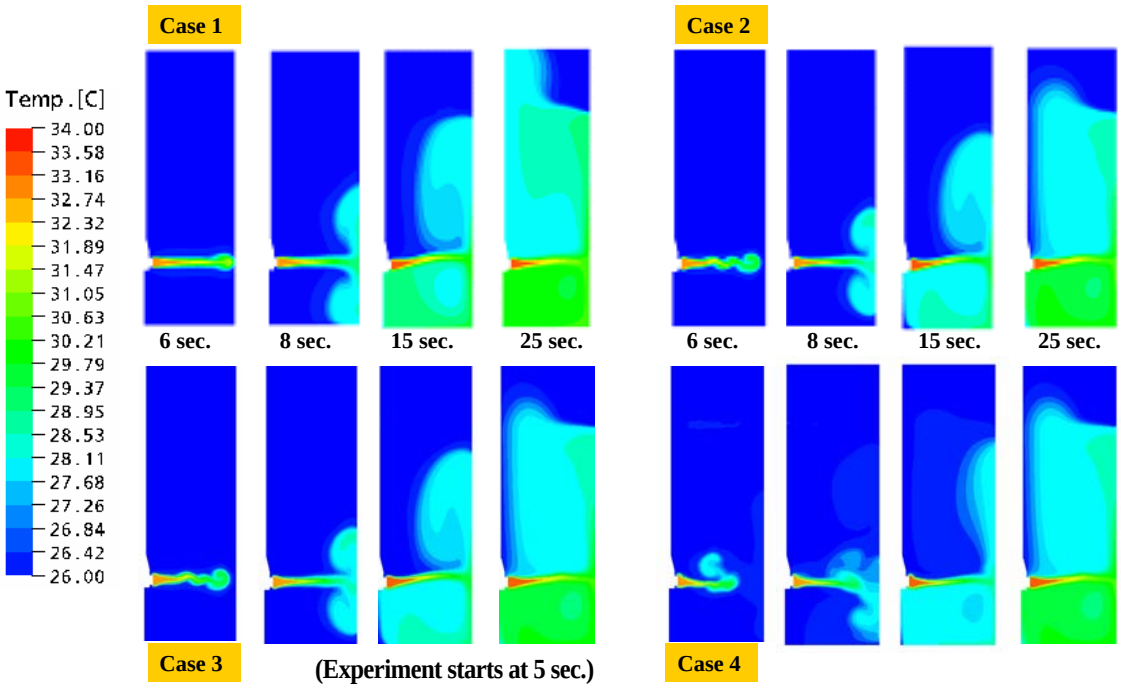

Fig. 8 Temperature Distribution of the CFD Results (Case 1~4)

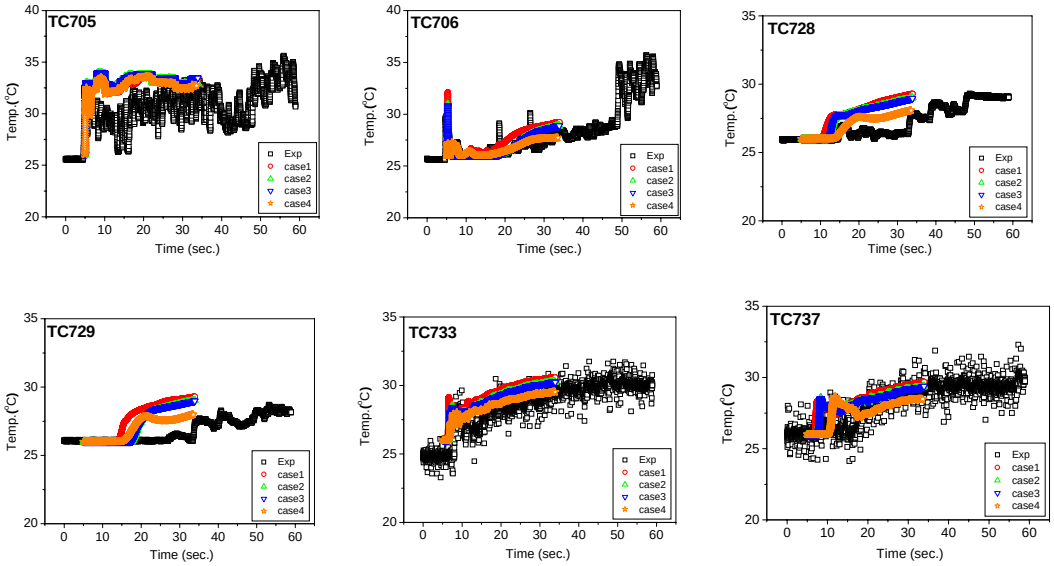

Fig. 9 Comparison of Test Data with CFD Results at Thermo-couple locations (Case 1~4)

Conclusions

When the steam of a high pressure and temperature was condensed and mixed with subcooled water in the tank, thermal mixing phenomenon was simulated with the steam condensation region model for a transient case of 30 seconds by CFX4.4. The condensation region model was developed based on the temperature distribution around the sparger discharge holes in the test results. The grid and numerical model sensitivity study was also performed to find the optimized methodology for thermal mixing analysis.

The comparison CFD results with the test data showed good agreement within 7~8% value. This difference may be arisen from that the temperature and the velocity of the calculated condensed water by the condensation region model are higher than the real value. Another reason may be the limit of condensation region model using the area average concept. This concept also neglects a three dimensional situation in the tank, while the CFX calculation was performed by the axisymmetry condition to save computation time. The sensitivity calculation results of CFD were very similar to each other at the region between the sparger and the tank wall irregardless of cases. However, the CFD results showed small different temperature distribution at the upper and lower region where the condensed water jet arrived after colliding with the tank wall. Especially for the high upper region, case 4 using the quick scheme predicted the test data better than other cases using the upwind scheme. Therefore, the numerical methods and grid meshes distribution for thermal mixing calculation should be carefully selected. However, the commercial CFD code of CFX4.4 together with the condensation region model can simulate the thermal mixing behavior reasonably well when a sufficient number of mesh distribution and a proper numerical method are adopted.

Acknowledgments

This work was financially supported for the nuclear R&D program from the Ministry of Science and Technology of Korea. The authors are sincerely grateful for the financial support.

References

1. C.-H. Song et al., 'Multi-dimensional Thermal-Hydraulic Phenomena in Advanced Nuclear Reactor Systems: Current Status and Perspectives of the R&D Program at KAERI', *Proc. NURETH-10*, Seoul, Korea, October 5-9, (2003).
2. Y.S. Kim et al, Steam Condensation Induced Thermal Mixing Experimental Using B&C Facility, KAERI Report, KAERI/TR-2933/ 2005 (2005).
3. C.K. Park et al, Steam Condensation Test Program and Analysis of Hydraulic Loads, KAERI Report, KAERI/TR-2946/2005 (2005).
4. H.S. Kang et al, A CFD Analysis of the Thermal Mixing Under the Transient of the Steam Discharging in a Subcooled Water Tank, KAERI Report, KAERI/TR-3008/2005 (2005).
5. H.S. Kang et al., " Numeriacl Study on the Local Temperature in IRWST Pool," *Proc. of ICONE-10*, Arlington, U.S.A, April (2002).
6. H.S. Kang et al., " CFD Analysis for Thermal Mixing Phenomena in the Subcooled Water Tank," *NTHAS4*, Sapporo, Japan, Dec. (2004).
7. KEPCO, *APR1400 Standard Safety Analysis Report*, (2002).
8. "Suppression Pool Temperature Limits for BWR Containments," U.S. NRC, (1981).
9. Ra, I.S., *IRWST Thermal Hydraulic Load Analysis Report*, N-001-END461-201,(1999).
10. Ansys, Inc., CFX4.4 Manual (2004).
11. J. Davis & G. Yadogaroglu, "Direct Contact Condensation in Himenz Flow Boundary Layers," Int. J. of Heat and Mass Transfer, 47, (2004), p.1863-1875.
12. Cook, D.H., "Pressure Suppression Pool Thermal Mixing," *NUREG-3471*, (1994).
13. H.S. Kang et al, Thermal Mixing Test Data Base Document, KAERI Report, KAERI/THETA-TM1, Rev.0, (2006).
14. J.C. Weimer et al, "Penetration of Vapor Jets Submerged in Subcooled Liquids", *AIChE J.*, Vol. 19, No. 3, (1989), p. 639-654.
15. H.Y. Kim, et al, A Study on the Characteristics of Direct Contact Condensation of a Steam jet Discharging into a Quenching Tank through a Single Horizontal Pipe, Ph.D Thesis, KAIST, (2001).
16. Frank M. White, V*iscous Fluid Flow 2nd*, Mcgraw-Hill, Inc., (1991), p.470-476.
17. Neil E. Todreas & Mujid S. Kaimi, *Nuclear System I*, Hemisphere Publishing Coperation, (1990) p.507-517
18. Gordon J. Van Wylen and Richard E. Sonntag, Fundamentals of Classical Thermodynamics *3rd.*, John Wiley & Sons, (1985), p.574-588.
19. H. K. Versteeg and W. Malalasekera, *An Inriduction to Computational Fluid Dynamics The Finite Volume Method*, Longman, (1995), p.118-134.
20. S. W. Bae and H. J. Sung, "Breakdown of the Reynolds Analogy in a Stagnation Region Under Inflow Disturbances," Theoretical and Computational Fluid Dynamics, Vol. 14, (2001), p.377-398.